

Manipulation of spin orientation via ferroelectric switching in Fe-doped Bi_2WO_6 from first principles

Katherine Inzani*,^{1,2} Nabaraj Pokhrel*,³ Nima Leclerc,^{2,4} Zachary Clemens,⁵
Sriram P. Ramkumar,⁵ Sinéad M. Griffin,^{1,2} and Elizabeth A. Nowadnick⁵

¹*Materials Science Division, Lawrence Berkeley National Laboratory, Berkeley, CA 94720, USA*

²*Molecular Foundry, Lawrence Berkeley National Laboratory, Berkeley, CA 94720, USA*

³*Department of Physics, University of California, Merced, CA 95343, USA*

⁴*Department of Electrical and Systems Engineering,*

University of Pennsylvania, Philadelphia, PA 19104, USA

⁵*Department of Materials Science and Engineering,*
University of California, Merced, CA 95343, USA

(Dated: December 9, 2021)

Atomic-scale control of spins by electric fields is highly desirable for future technological applications. Magnetically-doped Aurivillius-phase oxides present one route to achieve this, with magnetic ions substituted into the ferroelectric structure at dilute concentrations, resulting in spin-charge coupling. However, there has been minimal exploration of the ferroelectric switching pathways in this materials class, limiting predictions of the influence of an electric field on magnetic spins in the structure. Here, we determine the ferroelectric switching pathways of the end member of the Aurivillius phase family, Bi_2WO_6 , using a combination of group theoretic analysis and density functional theory calculations. We find that in the ground state $P2_1ab$ phase, a two-step switching pathway via $C2$ and Cm intermediate phases provides the lowest energy barrier. Considering iron substitutions on the W-site in Bi_2WO_6 , we determine the spin easy axis. By tracking the change in spin directionality during ferroelectric switching, we find that a 90° switch in the polarization direction leads to a 112° reorientation of the spin easy axis. The low symmetry crystal-field environment of Bi_2WO_6 and magnetoelastic coupling on the magnetic dopant provide a route to spin control via an applied electric field.

I. INTRODUCTION

Multiferroic materials with coupled ferroic orderings (e.g. ferromagnetism, ferroelectricity, ferroelasticity) exhibit intriguing physics and hold potential for enabling new types of future electronic devices.¹ In magnetoelectric materials with coupled ferroelectricity and magnetism, the ability to switch the magnetization by an applied electric field is particularly promising for low-power spintronics.² Materials approaches to multiferroicity, for example multiferroic superlattices³, nanocomposites⁴, domain walls⁵ and single phase materials⁶, typically focus on realizing long-range magnetic order for macroscopic devices. However, several recent works have pushed towards the fundamental limits of multiferroic phenomena, including electric field manipulation of molecular magnets^{7,8}, tuning exchange in a molecular system⁹, and the coherent electric field control of dilute iron dopants in a ferroelectric crystal.¹⁰ These milestones towards full control of isolated spins by electric fields may enable new functionalities in classical electronic devices in the field of spintronics as well as in quantum computing.^{10,11}

A promising pathway to achieve isolated spin centers with magnetoelectric coupling is to dope a ferroelectric structure with dilute concentrations of magnetic ions.¹⁰ Here, magnetoelectricity arises by coupling the ferroelectric's polar distortion with the spin dopant through spin-orbit interactions. This approach confers the rich phase space of ferroelectric crystals, in particular of complex

oxide materials, for use as hosts for spin dopants. In particular, the versatile structural motifs and distortions in ferroelectric oxides provide a highly tunable local environment for the spin center, allowing control of the magnetocrystalline properties via the crystal field environment. The symmetry lowering caused by the ferroelectric distortion results in magnetocrystalline anisotropies that lead to preferential alignment of spins within a plane (spin easy plane) or along an axis (spin easy axis). Using the prototypical ferroelectric PbTiO_3 as a host for Fe^{3+} spins, some of the present authors recently demonstrated that the tetragonal polar distortion results in a spin easy plane with 90° switching under the application of an electric field.¹⁰ However, preferentially aligning spins along an easy axis and 180° switching would have technical advantages for applications. Ferroelectric hosts providing lower crystallographic symmetries in the vicinity of the spin are more likely to support spin easy axes due to their highly distorted crystal fields, and so are sought for such ferroelectric-mediated spin switching.

The Aurivillius phases are a family of layered ferroelectric materials with low symmetry crystal structures that could satisfy these requirements. The Aurivillius structure is composed of m perovskite-like layers $(A_{m-1}B_mO_{3m+1})^{2-}$ interspersed with fluorite-like $(\text{Bi}_2\text{O}_2)^{2+}$ layers, giving the overall general formula $\text{Bi}_2A_{m-1}B_mO_{3m+3}$. The Aurivillius phases are well known for their robust ferroelectricity, including high Curie temperatures (T_c), large spontaneous polarizations¹²⁻¹⁴, and fatigue resistance.¹⁵ Furthermore, the

composition has great versatility owing to the different cations that can be placed on the A and B sites, which has led to efforts to design multiferroic Aurivillius compounds via incorporation of magnetic ions.^{16–22} Most work has focused on achieving long range magnetic ordering in single phase materials with large proportions of magnetic cations, for example in doped $\text{Bi}_{n+1}\text{Fe}_{n-3}\text{Ti}_3\text{O}_{3n+3}$ compounds. However, the complex crystal structure and difficulty in synthesis of phase pure samples has made characterization of the multiferroic properties difficult.^{21,23,24} In particular, the ferroelectric and magnetoelectric switching mechanisms have not been elucidated.²⁵ These limitations hinder the prediction of the behavior of magnetic spins during switching. Moreover, to the best of our knowledge, magnetoelectric coupling of isolated magnetic dopants has not yet been investigated in this class of materials.

Here, we use group theoretic analysis and first principles calculations to explore ferroelectric switching and control of magnetic dopants in the end member of the Aurivillius family, Bi_2WO_6 ($m=1$, $B=\text{W}$). We select Bi_2WO_6 because it exhibits robust ferroelectricity and also possesses a complex crystal structure which can provide a low symmetry crystallographic environment for magnetic dopants. Theoretical and experimental work has revealed that ferroelectricity in Bi_2WO_6 arises from an instability to a polar distortion involving large Bi displacements with respect to the perovskite layer.^{26–30} It undergoes a two-step paraelectric-ferroelectric phase transition sequence: at room temperature, Bi_2WO_6 crystallizes in the orthorhombic ferroelectric phase $P2_1ab$, then transitions to the polar orthorhombic structure $B2cb$ at 670°C, and finally transitions to the paraelectric monoclinic phase $A2/m$ above 950°C.³¹

Experiments have reported that ferroelectric switching in Bi_2WO_6 proceeds via a two-step process²⁹, but the details of the precise switching pathway taken are still lacking. We therefore start by determining the likely ferroelectric switching pathway, by systematically enumerating and then evaluating the energetics of several possible symmetry-distinct paths. Here we consider *intrinsic* ferroelectric switching paths, where we calculate energy barriers for coherent polarization reversal in a single infinite domain.³² Although this does not provide a full description of the dynamic ferroelectric switching process, work on other ferroelectrics^{33,34} has shown that when multiple symmetry-distinct switching paths are available, intrinsic barriers can correctly identify the experimental switching path. We then introduce Fe^{3+} dopants into the structure at dilute concentrations and track the change in spin directionality with ferroelectric switching. This work lends understanding to the magnetoelectric effects on isolated spins in Bi_2WO_6 , demonstrating the potential for atomic-scale spin control in this class of materials.

II. COMPUTATIONAL METHODOLOGY

We perform density functional theory (DFT) calculations using the Vienna *Ab initio* Simulation Package (VASP)^{35–38}, using projector augmented wave (PAW) pseudopotentials^{39,40} including Bi $5d^{10}6s^26p^3$, W $5p^65d^46s^2$, O $2s^22p^4$ and Fe $3d^64s^2$ as valence electrons. A plane wave cut-off energy of 800 eV is used with a $6 \times 6 \times 2$ Gamma-centered k -point grid (for the $P2_1ab$ Bi_2WO_6 36-atom unit cell), which converges the total energy to 1 meV per formula unit (f.u.). The same k -point grid is used for all undoped structures, and a $2 \times 2 \times 2$ k -point grid is used for the doped supercells. All calculations are done using the generalized gradient approximation (GGA) based exchange-correlation functional PBEsol⁴¹, which gives lattice parameters within 1% of experiment³⁰ ($a=5.443$ Å, $b=5.443$ Å, $c=16.557$ Å, for $P2_1ab$).

For undoped structures, we allow the ionic positions, cell volume, and cell shape to optimize and apply a force tolerance convergence of $1 \text{ meV } \text{\AA}^{-1}$. The nudged elastic band (NEB) method⁴² implemented in VASP is employed to find the structural parameters and energies of intermediate structures lying along the ferroelectric switching pathways. For the NEB calculations, the force convergence tolerance is increased to $10 \text{ meV } \text{\AA}^{-1}$.

We calculated Fe^{3+} substitutional defects on W-sites in $2 \times 2 \times 1$ supercells of Bi_2WO_6 (144 atoms), with three electrons added for charge compensation. For structures containing more than one symmetrically inequivalent W-site, we consider each as a different dopant site. An effective Hubbard term $U_{\text{eff}} = U - J = 4 \text{ eV}$ is added to the Fe d -orbitals within the Dudarev approach.⁴³ Geometry optimization of the ions for each defect supercell is completed to a force convergence of $10 \text{ meV } \text{\AA}^{-1}$, whilst keeping the cell volume and shape fixed. Magnetocrystalline anisotropy energy (MCAE) surfaces are calculated by including spin-orbit coupling self consistently and varying the spin quantization axes over 194 points. We make use of the ISOTROPY software suite⁴⁴ for group theoretic analysis and VESTA⁴⁵ for the visualization of crystal structures.

III. RESULTS AND DISCUSSION

A. Ground state crystal structure

To set the stage for understanding ferroelectric switching, we first analyze the structural distortions present in the ferroelectric $P2_1ab$ structure. The $P2_1ab$ space group is established by the condensation of three distinct structural distortions that transform like irreducible representations (irreps) of the high-symmetry reference structure $I4/mmm$ (Fig. 1a, b). These distortions are a

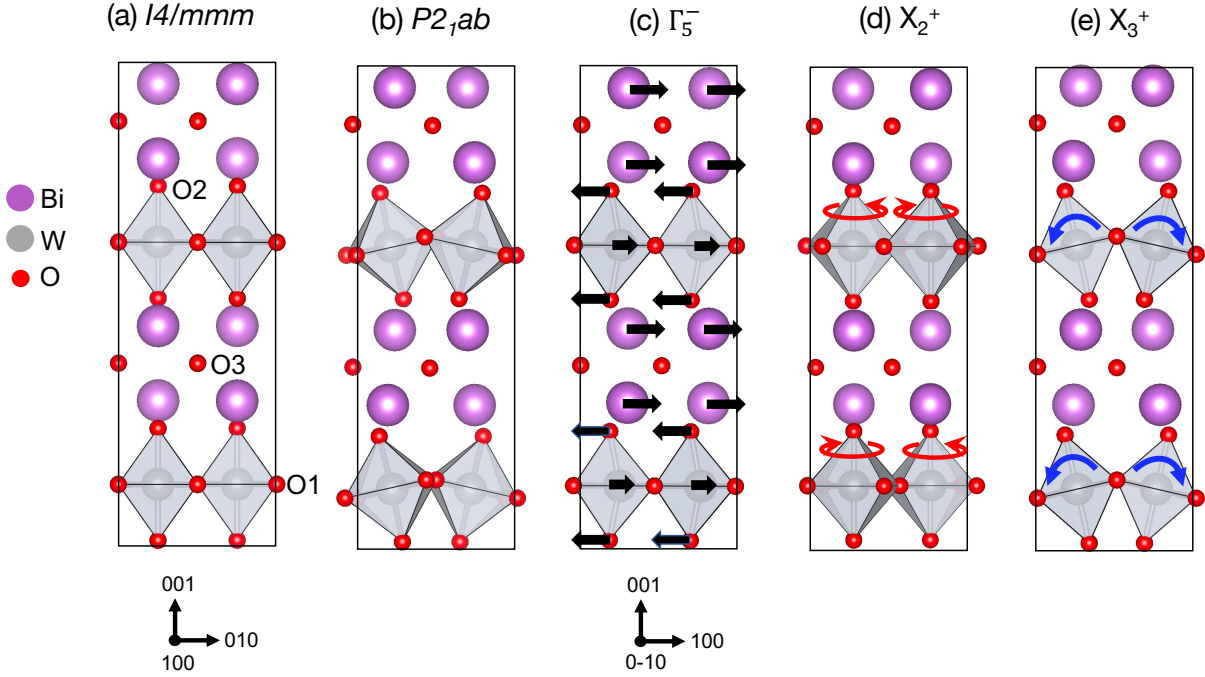


FIG. 1. The (a) high-symmetry reference structure $I4/mmm$ and (b) polar orthorhombic structure $P2_1ab$ of Bi_2WO_6 . A structural decomposition of $P2_1ab$ into symmetry adapted modes of $I4/mmm$ reveals three main structural distortions: (c) a polar displacement along $[1\ 0\ 0]$ with symmetry Γ_5^- , (d) an octahedral rotation about $[0\ 0\ 1]$ with symmetry X_2^+ , and (e) an out-of-phase octahedral tilt about $[1\ 0\ 0]$ with symmetry X_3^+ . The axes shown under panel (a) are used for all panels except for (c).

polar displacement along the $[1\ 0\ 0]$ orthorhombic axis which transforms like the irrep Γ_5^- , an octahedral rotation about $[0\ 0\ 1]$ which transforms like X_2^+ , and an out-of-phase ($a^-a^-c^0$ in Glazer notation⁴⁶) octahedral tilt about $[1\ 0\ 0]$ which transforms like X_3^+ , (Fig. 1c-e). The amplitudes of these three distortions, computed from DFT-relaxed and experimental structures, are reported in Table I. Overall the distortion amplitudes show good agreement between DFT and experiment. The main contribution to the polar distortion comes from displacement of the Bi cations against the O2 atoms as shown in Fig. 1(c). In addition to the three distortions discussed above, there are several other distortions which are symmetry-allowed in the $P2_1ab$ structure, but they have negligible amplitudes²⁸ so we do not consider them in this work.

B. Ferroelectric switching pathways

To provide a framework for systematically identifying ferroelectric switching pathways, we next enumerate possible metastable structural phases of Bi_2WO_6 and compute their energies with DFT. The key to uncovering the metastable structural phases is to recognize that each of the three structural distortions shown in Figure 1 is described by a two-dimensional order parameter $Qe^{i\alpha}$.³⁴ Here Q is the order parameter amplitude and α is the

TABLE I. Decomposition of the Bi_2WO_6 $P2_1ab$ structure (DFT-relaxed and experimental) into symmetry adapted modes of $I4/mmm$. The experimental structure is taken from Ref. 47. The amplitudes are given in Å for a 36-atom computational cell. For the O1 atoms, the coordinates in parentheses indicate the axes along which the atoms displace; there are two distinct O1 displacement patterns in the xy plane that are consistent with the symmetry.

Atom	Γ_5^-		X_2^+		X_3^+	
	DFT	Expt.	DFT	Expt.	DFT	Expt.
Bi	0.66	0.68	0	0	0.33	0.30
W	0.18	0.25	0	0	0	0
O1(z)	0	0	0	0	0.87	0.70
O1(xy)	-0.15	-0.11	0.75	0.85	0	0
O1(xy)	-0.25	-0.29	-0.01	-0.02	0	0
O2	-0.77	-0.74	0	0	-1.10	-0.89
O3	0.27	0.17	0	0	-0.05	-0.02
Total	1.10	1.09	0.75	0.85	1.44	1.17

phase. For the X_3^+ octahedral tilt and the Γ_5^- polar distortion, the phase α describes the orientation of the tilt (polar) axis. For the X_2^+ octahedral rotation, the phase describes the relative “sense” of the octahedral rotations in adjacent perovskite layers.

Each two-dimensional structural order parameter can lie along three symmetry-distinct directions ($Q \cos \alpha$, $Q \sin \alpha$) = $(a, 0)$, (a, a) , or (a, b) where $a \neq b$ are real num-

TABLE II. Subgroups of $I4/mmm$ established by different combinations of the X_3^+ , X_2^+ , and Γ_5^- order parameter directions. Total energies, distortion amplitudes, and lattice parameters obtained from DFT structural relaxations of Bi_2WO_6 in each space group are given. The energies are reported relative to the energy of $P2_1ab$, which is set to 0 meV/f.u.. If a structure relaxes to a higher symmetry space group, that space group is indicated in the energy column. The distortion amplitudes are obtained by decomposing the distorted structures with respect to $I4/mmm$ and are reported for a 36-atom computational cell.

Irreps	Order parameter direction			Space group (N^o)	Amplitude (\AA)			Lattice parameters (\AA)			Energy (meV/f.u.)
	Γ_5^-	X_2^+	X_3^+		Γ_5^-	X_2^+	X_3^+	a	b	c	
-	-	-	-	$I4/mmm$ (139)	0	0	0	3.806	3.806	16.453	355.51
$X_2^+ \oplus X_3^+$	-	(b, 0)	(c, 0)	$P2_1/c$ (14)	0	0.91	1.30	5.331	5.353	8.697	158.72
	-	(b, 0)	(0, c)	$Pcab$ (61)	0	0.78	1.35	5.350	5.360	16.844	149.74
	-	(b, b)	(c, c)	$C2/m$ (12)	0	0.48	1.46	7.602	7.614	16.602	157.40
$\Gamma_5^- \oplus X_3^+$	(a, 0)	-	(c, c)	$Cm2a$ (39)	0.44	0	1.53	7.601	7.754	16.481	103.46
	(a, a)	-	(0, c)	$B2cb$ (41)	1.19	0	1.60	5.467	5.472	16.553	4.38
	(a, a)	-	(c, 0)	$Bb2_1m$ (36)							($Fmm2$)
$\Gamma_5^- \oplus X_2^+$	(a, a)	(b, 0)	-	$Bb2_1m$ (36)	0.98	1.24	0	5.389	5.395	16.481	67.05
	(a, a)	(0, b)	-	$Cm2a$ (39)	1.01	1.22	0	7.601	7.754	16.481	71.21
	(a, 0)	(b, b)	-	$Cm2m$ (38)	1.15	0.74	0	7.544	7.845	16.569	133.20
$\Gamma_5^- \oplus X_2^+ \oplus X_3^+$	(0, a)	(b, b)	(c, c)	Cm (8)	0.45	0.53	1.46	7.729	7.584	16.506	99.06
	(a, 0)	(b, b)	(c, c)	$C2$ (5)	0.49	0.58	1.45	7.570	7.740	16.507	96.68
	(a, a)	(b, 0)	(c, 0)	$P2_1$ (4)							($Bb2_1m$)
	(a, a)	(0, b)	(0, c)	Pc (7)	1.11	0.76	1.44	5.442	5.443	8.688	-0.08
	(a, a)	(b, 0)	(0, c)	$P2_1ab$ (29)	1.11	0.75	1.44	5.443	5.443	16.557	0

bers and each direction establishes a different subgroup of $I4/mmm$. For example, the $P2_1ab$ space group is established by condensing the X_3^+ , X_2^+ , and Γ_5^- distortions along the (0,a), (a,0) and (a,a) order parameter directions, respectively. Taking these order parameters to lie along different combinations of directions generates structures of different symmetries. In Table II we consider all other possible combinations of the X_3^+ , X_2^+ , and Γ_5^- order parameter directions, and enumerate the space groups that these generate (we do not include the low symmetry (a,b) direction in this enumeration because structures defined by this direction generally return to a higher symmetry direction upon DFT relaxation). Table II also shows space groups that are generated by combining two out of the three order parameters taken along different combinations of directions. Space groups generated by each order parameter individually are given in Appendix A.

We then perform structural relaxations of Bi_2WO_6 with its symmetry constrained to each space group identified in Table II, and report the resulting energy and structural parameters. Most metastable structures have energies ranging from ≈ 65 to ≈ 160 meV per f.u. above $P2_1ab$. We find two very low energy structures: $B2cb$ (4.38 meV/f.u.) and Pc which we find to be slightly lower in energy than $P2_1ab$. The Pc and $P2_1ab$ structures exhibit the same X_3^+ and Γ_5^- distortions, the only difference is the relative “sense” of the X_2^+ rotations in adjacent perovskite layers, thus it is unsurprising that these phases are very close in energy. We note that the relative energy of Pc and $P2_1ab$ is quite sensitive to the value of the lattice parameters. For example, Ref. 28

found Pc to be about 3 meV/f.u. higher in energy than $P2_1ab$ from DFT calculations with the LDA functional. Since $P2_1ab$ is the experimentally reported ground state, we do not further consider the Pc phase here.

We next use the results of Table II to enumerate possible Bi_2WO_6 ferroelectric switching pathways. The simplest way to reverse the polarization is in a single 180° step, where the polarization is brought to zero and then turned on again pointing in the opposite direction, as shown in Figure 2a. At the midpoint of the path, the amplitude of the polarization is zero, and the symmetry of the crystal structure is $Pcab$, which is 149.74 meV/f.u. above the $P2_1ab$ ground state structure (see Table II). The $Pcab$ crystal structure is shown in Figure 3a.

In addition to the one-step $Pcab$ switching path, we identify three “two-step” switching pathways, where the polarization reverses direction by rotating through two 90° steps (while maintaining finite amplitude). Since the Γ_5^- order parameter in $P2_1ab$ is oriented along the (a,a) direction, rotating it by 90° takes it to either the $(-a,a)$ or $(a,-a)$ direction. This rotation requires that the Γ_5^- order parameter pass through the (0,a) or (a,0) direction. Table II reveals that the $Cm2a$, $Cm2m$, $C2$, and Cm structures satisfy this requirement. Interestingly, the energies of $Cm2a$, $C2$, and Cm are all near 100 meV/f.u. (within 10 meV/f.u. of each other), whereas $Cm2m$ is somewhat higher (133.20 meV/f.u.). Due to its higher barrier, we do not consider the $Cm2m$ pathway further in this work.

Using these identified structures, we construct the two lowest energy two-step ferroelectric switching pathways in Figure 2(b-c). Figure 2(b) shows a pathway that

passes through $Cm2a$ twice as the polarization rotates in two 90° steps. At the midpoint of the switching path, the structure passes through an orthorhombic twin domain of $P2_1ab$. Note that the structure passes through different domains of $Cm2a$ in the first and second steps. As the polarization rotates counterclockwise, the X_3^+ order parameter rotates clockwise by 90° in the first step, and then rotates back to its original orientation in the second step. In each step, the X_2^+ order parameter turns off so that it reaches zero at the $Cm2a$ structure, and then turns on again reoriented by 90° . The $Cm2a$ structure is shown in Figure 3(b). Here the (a,a) direction of X_3^+ establishes an octahedral tilt pattern where the tilt axes of adjacent perovskite layers are perpendicular to each other, so that there are $a^-b^0b^0$ and $b^0a^-b^0$ rotations in the dark and light grey perovskite layers in Figure 3(b), respectively. Note that the higher energy $Cm2m$ pathway follows a similar evolution of structural order parameters as the $Cm2a$ path, except the X_2^+ rather than the X_3^+ order parameter rotates during the switching process.

The second two-step switching path that we investigate is shown in Figure 2(c). The Γ_5^- and X_3^+ order parameters follow the same sequence as in Figure 2(b), except now the X_2^+ order parameter makes two 90° rotations while maintaining finite amplitude, rather than turning off/on. The barrier structure in the first step has symmetry $C2$, whereas in the second step it has symmetry Cm . The $C2$ and Cm structures are shown in Figure 3(c) and (d), respectively. These structures have the same $a^-b^0b^0/b^0a^-b^0$ octahedral tilt pattern as $Cm2a$. The $C2$ and Cm structures share the same X_2^+ rotation pattern, where every other perovskite layer (those colored green in Figure 3(c-d)) exhibit finite amplitude rotations about $[0\ 0\ 1]$, and the other (grey) layers have no X_2^+ rotation amplitude. The difference between the $C2$ and Cm structures is the orientation of the polarization with respect to the X_3^+ and X_2^+ order parameters: in $C2$ the polarization lies along the X_3^+ tilt axis of the green octahedra which have finite X_2^+ rotations, whereas in Cm the polarization lies along the X_3^+ tilt axis of the grey octahedra which have no X_2^+ rotation.

In order to investigate how the energy changes during switching, Figure 2(d) shows nudged elastic band (NEB) calculations of the energy as a function of switching coordinate for the paths in Figure 2(a-c). Both two-step paths have a significantly lower energy barrier than the one-step $Pcab$ path, with the energy barriers for the $C2/Cm$ path (96.68 and 99.06 meV/f.u. in the first and second steps, taken from Table II) being slightly lower than the $Cm2a$ path (103.46 meV/f.u.).

Figure 4 shows how the amplitudes of the X_3^+ , X_2^+ , and polar Γ_5^- distortions evolve along each ferroelectric switching path, obtained from NEB calculations. In the one-step switching path shown in Figure 4(a), the polar distortion amplitude goes to zero at the barrier structure $Pcab$, whereas the X_2^+ and X_3^+ distortion amplitudes remain almost unchanged throughout the switching process.

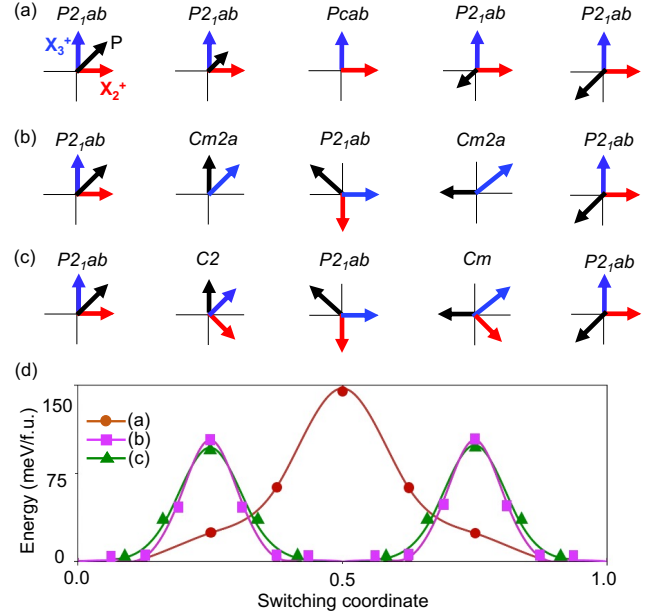


FIG. 2. Ferroelectric switching pathways in Bi_2WO_6 . (a)-(c) show how the X_3^+ , X_2^+ , and Γ_5^- (\mathbf{P}) order parameters, denoted by blue, red, and black arrows, respectively, evolve along the switching path. Path (a) is a one-step path, whereas paths (b)-(c) are two-step paths which pass through an orthorhombic twin of $P2_1ab$ at the midpoint of the switching path. (d) Energy as a function of switching coordinate for the paths shown in (a)-(c).

In the two-step switching path via $Cm2a$ shown in Figure 4(b), at the $Cm2a$ barrier the polar distortion amplitude decreases by about half and that of X_2^+ amplitude goes to zero, whereas the X_3^+ amplitude again changes very little throughout the switching process. Finally, for the two-step $C2/Cm$ path shown in Figure 4(c), all three distortion amplitudes remain finite throughout the switching process, although the polar and X_2^+ amplitudes are suppressed upon approaching the $C2/Cm$ barriers.

To summarize, we find that the two-step switching paths have lower energy barriers than the one-step switching path in Bi_2WO_6 . This implies that switching proceeds via two 90° steps, in agreement with the experimental observations of Ref. 29. We find that the two-step paths that pass through $Cm/C2$ and $Cm2a$ have almost the same energy barrier (≈ 100 meV/f.u.), with the barrier for the $Cm/C2$ path being slightly lower. We also investigate the epitaxial strain dependence of these energy barriers (Appendix B), and find that the two-step barriers remain the lowest energy except possibly under highly compressive strains. The two-dimensional structural order parameters facilitate the lower energy two-step switching, which involves order parameter rotation rather than completely turning the polarization off/on. We make use of these ferroelectric switching paths in the next section to guide us to the relevant structural

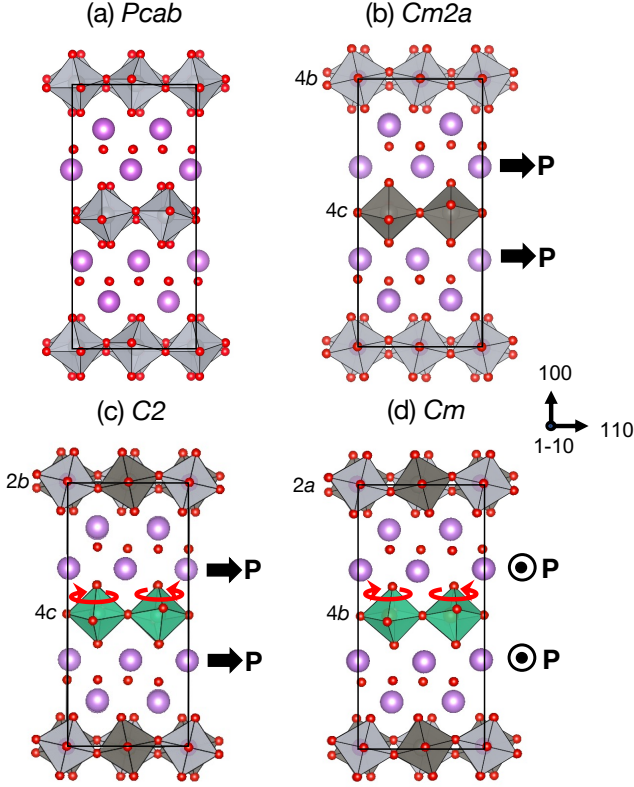


FIG. 3. Barrier structures of Bi_2WO_6 realized along the ferroelectric switching paths. The $\text{Cm}2a$ structure (b) has two distinct W Wyckoff positions, indicated by the light grey (4b) and dark grey (4c) octahedra. The $\text{C}2$ structure (c) also has two distinct W Wyckoff positions, indicated by grey (2b) and green (4c) octahedra, and two symmetrically inequivalent W-sites on the 2b position indicated in light and dark grey, respectively. Similarly, the Cm structure (d) has two distinct W Wyckoff positions, indicated by grey (2a) and green (4b) octahedra, and two symmetrically inequivalent W-sites on the 2a position indicated in light and dark grey, respectively.

phases in which to explore the spin orientation of magnetic dopants in Bi_2WO_6 .

C. Spin directionality of magnetic dopants

We next investigate the impact of polarization reversal on the spin orientation of magnetic dopants in Bi_2WO_6 . Magnetic dopants in Bi_2WO_6 exhibit magnetocrystalline anisotropy – a preferred directionality of the unpaired electron spins – that arises due to the crystal field at the dopant site and spin-orbit coupling. Here, we consider Fe^{3+} substitutional defects on W-sites, which is one of the potential defect species in Bi_2WO_6 . Although the $P2_1ab$ structure only contains one distinct W site, the barrier structures encountered in the two-step switching processes contain multiple symmetry-distinct W sites (and hence dopant positions), which are shown in Figure 3(b-d). The energetics of this defect and alternative

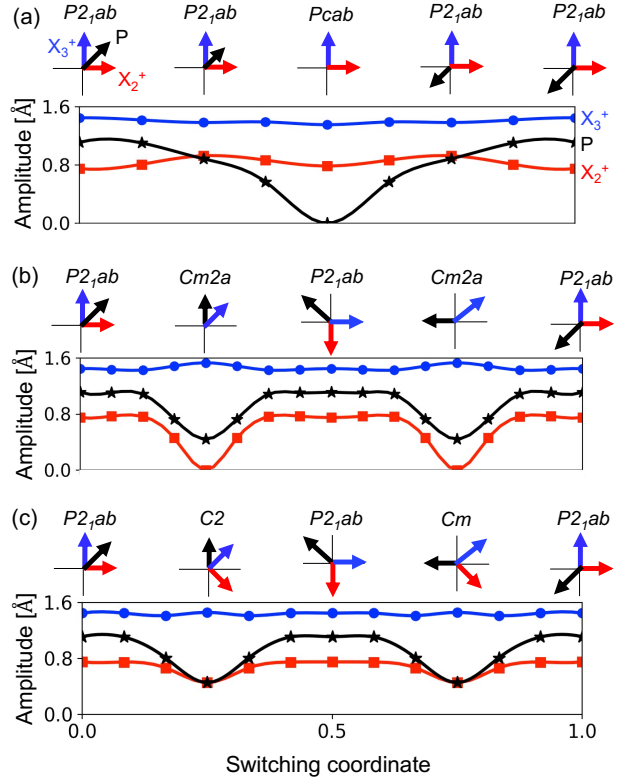


FIG. 4. Amplitudes of the X_3^+ , X_2^+ , and Γ_5^- (\mathbf{P}) structural distortions as a function of switching coordinate for each of the switching paths shown in Figure 2: (a) one-step switching with barrier $Pcab$, (b) two-step switching with barrier $\text{Cm}2a$, and (c) two-step switching with barriers $\text{C}2/\text{Cm}$. The amplitudes are obtained from NEB calculations and are reported for a 36-atom computational cell.

Fe-sites will be fully considered in a forthcoming work.

Figure 5 tracks the change in the MCAE surface along the two lowest energy switching pathways, $P2_1ab \rightarrow \text{C}2 \rightarrow P2_1ab$ and $P2_1ab \rightarrow \text{Cm}2a \rightarrow P2_1ab$, revealing the change in directionality of the Fe-dopant spins during switching. Beginning in the $P2_1ab$ phase with the polarization \mathbf{P} oriented along $[1\ 0\ 0]$, we identify a spin easy axis that lies in the crystallographic ab -plane at 11° with respect to \mathbf{P} . In the octahedral orientation indicated in the first step, the spin easy axis is along $(1.0, -0.2, 0.0)$. The calculated magnitude of the MCAE is $530\ \mu\text{eV}$, which is the energy difference between the x and z principal axes of the MCAE surface. In addition, we calculate an in-plane anisotropy between the x and y principal axes of $130\ \mu\text{eV}$. The principal axes of the MCAE surface for each of the switching steps are given in Appendix C.

Taking the $\text{Cm}2a$ path (Figure 5a), the Fe-dopant (along with all the octahedra in the top layer) first passes through the 4c Wyckoff position in $\text{Cm}2a$, which has site symmetry m . On this site the MCAE is significantly increased to $940\ \mu\text{eV}$ and the spin easy axis is $(-0.7, 0.7, 0.0)$. At 90° switching, the structure re-

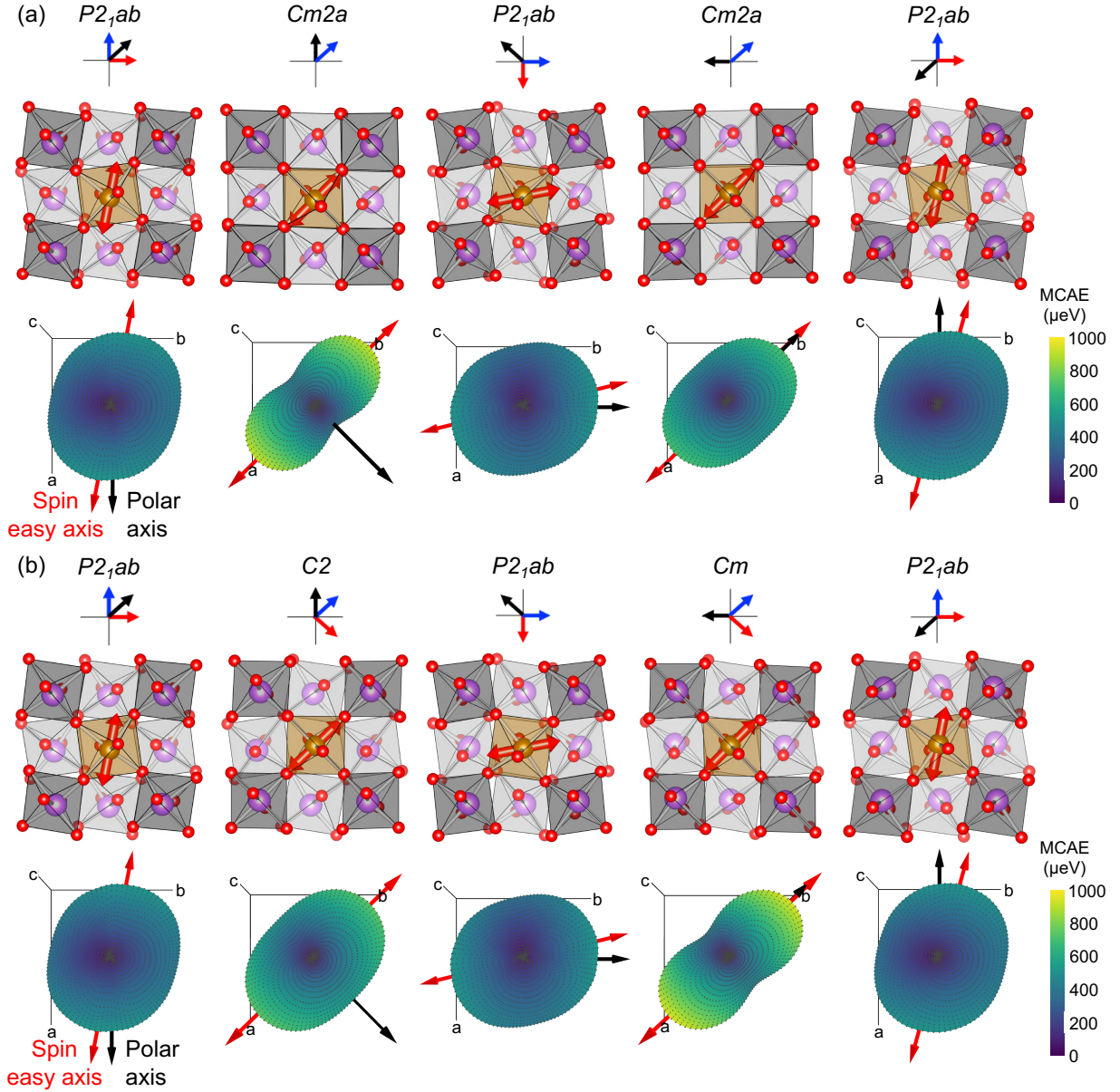


FIG. 5. Change in spin directionality on an Fe-dopant during switching (a) via the $Cm2a$ intermediate phase and (b) via the $C2$ and Cm phases. Magnetocrystalline anisotropy energy surfaces are plotted with red arrows indicating the spin easy directions and black arrows showing the polar axis in the $P2_1ab$ phases. In the crystal structures, purple, red and gold spheres are W, O and Fe respectively, and only WO_6 octahedra are shown; the Fe-dopant sits in the upper layer with the dark grey octahedra and the lower layer is light grey.

turns to the $P2_1ab$ phase with spin easy axis now along $\langle -0.2, 1.0, 0.0 \rangle$, a rotation of 112° around the c -axis from the original spin easy axis. Passing through the $Cm2a$ structure a second time, the dopant (and all octahedra in the top layer) is in the $4b$ Wyckoff position with site symmetry 2, resulting in a slightly lower MCAE of $730 \mu\text{eV}$ compared to the $4c$ site, although the spin easy axis remains the same. This can be understood by the variation in off-centering of Fe, making a 170° O–Fe–O bond angle in the $4c$ position compared to 180° in the $4b$ position (taking the bonds aligned parallel to the spin

axis). In the last step, the structure returns to $P2_1ab$ with \mathbf{P} switched by 180° and the spin easy axis returned to $\langle 1.0, -0.2, 0.0 \rangle$. (Beginning in one of the orientations in the lower layer, the Fe-dopant would pass through the $4b$ Wyckoff position first and the $4c$ position second.)

Alternatively, taking the $C2/Cm$ path (Figure 5b), the Fe-dopant first passes through the $C2$ phase in Wyckoff position $2b$ (site symmetry 2) and secondly through the Cm phase in Wyckoff position $2a$ (site symmetry m). The MCAE values are $750 \mu\text{eV}$ and $970 \mu\text{eV}$ respectively, and the spin easy axis is along $\langle -0.7, 0.7, 0.0 \rangle$ in both

TABLE III. Fe^{3+} dopant positions, site symmetries and magnetocrystalline anisotropy energies (MCAE) in $P2_1ab$ and intermediate switching phases. * indicates the site chosen for the switching pathway in Figure 5b, where multiple sites are available.

Phase	Wyckoff	Site	MCAE (μeV)	
	site	symmetry	Out-of-plane	In-plane
$P2_1ab$	4a	1	530	130
$Cm2a$	4b	2	730	210
	4c	m	940	510
Cm	2a*	m	970	520
	2a	m	980	530
	4b	1	650	130
$C2$	2b*	2	750	210
	2b	2	760	200
	4c	1	N/A	

cases. As in the $Cm2a$ path, a 90° switch in the polarization direction results in a rotation of the spin easy axis by 112° about the c -axis. The similarity in crystal field environment in the two switching pathways accounts for the resemblance between the MCAE surfaces in Figure 5a-b. Details of the site symmetries and in-plane and out-of-plane MCAE are listed in Table III, including alternative dopant positions. There are symmetrically inequivalent W-sites on the 2a Wyckoff position in Cm and the 2b position in $C2$, which have a slightly different crystal field environment from the sites considered above, resulting in small differences in the MCAE values. In addition, an alternative domain choice for the switching pathways could have taken the Fe-dopant through the 4b position in Cm and the 4c position in $C2$. MCAE data is not available for the latter as the structural optimization on this site did not converge the forces on the ions below a reasonable number.

The MCAEs reported here are typical of 3d transition metal atoms,^{48,49} and their low magnitudes indicate that thermally induced switching could occur if not kept at very low temperatures. This could be sufficient for devices operating at cryogenic temperatures (e.g. quantum computing); an MCAE of 0.5 meV corresponds to an energy barrier of ~ 6 K, three orders of magnitude greater than the typical mK operating temperatures of many quantum devices. However, strategies to increase the MCAE should be explored to exclude thermally induced switching in higher temperature applications. These could include systems with reduced dimensionalities and 4d or 5d transition metal and rare earth atoms which have been shown to exhibit giant MCAE values.⁵⁰⁻⁵³

CONCLUSION

We use a combination of group theoretic analysis and DFT calculations to determine the intrinsic ferroelectric switching pathways of Bi_2WO_6 . We identify several pathways: a one-step pathway, via $Pcab$, and three

two-step pathways, via $C2/Cm$, $Cm2a$ and $Cm2m$. By comparing energies of the barrier structures we find that the two-step paths are lower energy than the one-step path, in agreement with experiment:²⁹ in particular, the $C2/Cm$ path provides the lowest energy barrier of 97-99 meV/f.u. and the $Cm2a$ barrier is only slightly higher at 103 meV/f.u.. These intrinsic switching barrier energies are comparable to those of other structurally complex ferroelectrics such as LiNbO_3 and $\text{Ca}_3\text{Ti}_2\text{O}_7$, which have barriers of 130 meV/f.u.⁵⁴ and 64 meV/f.u.³⁴, respectively.

Magnetic defects experience a change in crystal field environment during switching, resulting in a change in magnetic anisotropy at each switching step. Contrasting with Fe^{3+} dopants in PbTiO_3 which exhibit a spin easy plane¹⁰, the lower crystallographic symmetry of Bi_2WO_6 results in a spin easy axis. By calculating MCAE surfaces, we find how the spin orientation of a Fe^{3+} substitutional defect on W-sites changes during polarization switching. In the $P2_1ab$ structure, the spin easy axis is in the ab -plane at 11° with respect to the polar axis and has an out-of-plane MCAE of 530 μeV and an in-plane MCAE of 130 μeV . During ferroelectric switching via intermediate phases, the spin easy axis rotates within the ab -plane and the MCAE is considerably increased (650-980 μeV out-of-plane, 130-530 μeV in-plane) due to changes in the local crystal environment of the dopant. We find that switching the polarization by 90° in Bi_2WO_6 results in a 112° rotation of the spin easy axis. However, a full 180° reversal of the polarization returns the spin easy axis to its original orientation.

Based on these results, we suggest that a possible pathway to achieve full spin control with 180° polarization switching is to consider ferroelectrics where an additional structural distortion that couples to the polarization must change during 180° switching. If this structural distortion also impacts the magnetic anisotropy, then the change to the distortion due to polarization switching may result in a different spin easy axis in the $+\mathbf{P}$ and $-\mathbf{P}$ states. For example, changes to octahedral rotation distortions, which are extremely common in (layered) perovskite oxides, can modify spin easy planes and axes.^{55,56} Although the X_3^+ and X_2^+ octahedral rotation patterns in Bi_2WO_6 change along the two-step switching paths, the octahedral rotation amplitudes and pattern in the starting ($+\mathbf{P}$) and final ($-\mathbf{P}$) structures are the same. However, there are other layered perovskite ferroelectrics, such as the Aurivillius compound $\text{SrBi}_2\text{Ta}_2\text{O}_9$ ⁵⁷ and several $n=2$ Ruddlesden-Popper ferroelectric oxides,^{34,58} where reversal of the polarization requires *by symmetry* that the sense of an octahedral rotation also reverse. Compounds such as these may provide the necessary ingredients to create distinct low symmetry environments and hence different MCAE surfaces in polarization reversed states.

ACKNOWLEDGEMENTS

This work was supported by the Microelectronics Co-Design Research Program, under the Office of Science of the U.S. Department of Energy under Contract No. DE-AC02-05CH11231 (K.I., N.L., and S.M.G.). N.P., Z.C., S.P.R., and E.A.N. acknowledge support from University of California, Merced. Computational resources were provided by the National Energy Research Scientific Computing Center and the Molecular Foundry, DOE Office of Science User Facilities supported by the Office of Science, U.S. Department of Energy under Contract No. DE-AC02-05CH11231. The work performed at the Molecular Foundry was supported by the Office of Science, Office of Basic Energy Sciences, of the U.S. Department of Energy under the same contract. We also acknowledge the use of computational resources supported by the Center for Functional Nanomaterials, which is a U.S. DOE Office of Science Facility, and the Scientific Data and Computing Center, a component of the Computational Science Initiative, at Brookhaven National Laboratory under Contract No. DE-SC0012704. In addition, this work used the Extreme Science and Engineering Discovery Environment (XSEDE) Expanse cluster at the San Diego Supercomputing Center through allocation TG-PHY200085.

AUTHOR CONTRIBUTIONS

K.I. and N.P. contributed equally to this work.

Appendix A: Additional subgroups of $I4/mmm$

Table A1 reports the subgroups of $I4/mmm$ generated by distinct directions of the Γ_5^- , X_2^+ , and X_3^+ order parameters, along with the distortion amplitudes, lattice parameters, and total energies of Bi_2WO_6 after DFT structural relaxations in each space group.

Appendix B: Epitaxial strain

Figure A1 presents the energies of the ferroelectric switching barrier structures discussed in the main text as a function of epitaxial strain. In these calculations, biaxial strain is applied in the ab -plane, and the lattice parameter c and all atomic positions are allowed to relax. We find that all energy barriers increase upon going from compressive to tensile strain. The $Pcab$ energy barrier changes the most dramatically with strain. The $C2/Cm$ structures provide the lowest energy barriers at all strains that we consider, although under highly compressive strains (larger than 2%) the $Pcab$ barrier may become lowest, which would suggest a crossover from two- to one-step switching being the lowest energy path.

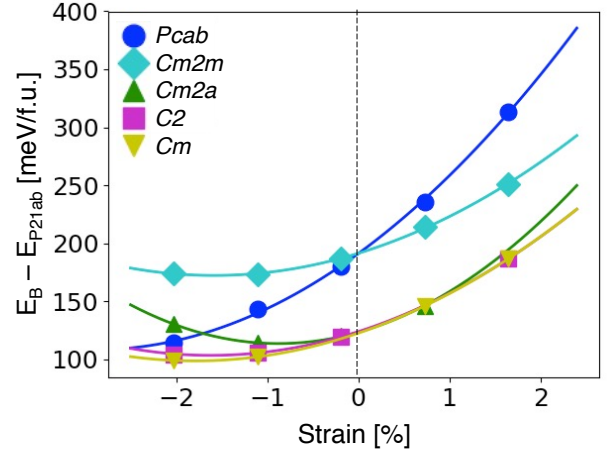


FIG. A1. Energy of the ferroelectric switching barrier structures B above $P21ab$ as a function of epitaxial strain. The strain is applied biaxially in the ab plane, and 0% strain is defined with respect to the $P21ab$ lattice parameters.

Appendix C: Principal axes of magnetocrystalline anisotropy energy surfaces

Table A2 reports the principal axes of the MCAE surfaces shown in Figure 5. These axes are orthonormal vectors which describe the three principal axes of rotation of the MCAE surface. The spin easy axis lies along the x principal axis.

- ¹ N. A. Spaldin and R. Ramesh, *Nat. Mater.* **18**, 203 (2019).
- ² S. Manipatruni, D. E. Nikonov, C. C. Lin, T. A. Gosavi, H. Liu, B. Prasad, Y. L. Huang, E. Bonturim, R. Ramesh, and I. A. Young, *Nature* **565**, 35 (2019).
- ³ J. A. Mundy, C. M. Brooks, M. E. Holtz, J. A. Moyer, H. Das, A. F. Rébola, J. T. Heron, J. D. Clarkson, S. M. Disseler, Z. Liu, A. Farhan, R. Held, R. Hovden, E. Padgett, Q. Mao, H. Paik, R. Misra, L. F. Kourkoutis, E. Arenholz, A. Scholl, J. A. Borchers, W. D. Ratcliff, R. Ramesh, C. J. Fennie, P. Schiffer, D. A. Muller, and D. G. Schlom, *Nature* **537**, 523 (2016).

- ⁴ R. Cai, V.-A. Antohe, Z. Hu, B. Nysten, L. Piraux, and A. M. Jonas, *Adv. Mater.* **29**, 1604604 (2017).
- ⁵ G. Catalan, J. Seidel, R. Ramesh, and J. F. Scott, *Rev. Mod. Phys.* **84**, 119 (2012).
- ⁶ J. Wang, J. B. Neaton, H. Zheng, V. Nagarajan, S. B. Ogale, B. Liu, D. Viehland, V. Vaithyanathan, D. G. Schlom, U. V. Waghmare, N. A. Spaldin, K. M. Rabe, M. Wuttig, and R. Ramesh, *Science* **299**, 1719 (2003).

TABLE A1. Subgroups of $I4/mmm$ established by distinct directions of the Γ_5^- , X_2^+ , and X_3^+ order parameters. Total energies, distortion amplitudes, and lattice parameters obtained from DFT structural relaxations of Bi_2WO_6 in each space group are given. The energies are reported relative to the energy of $P2_1ab$, which is set to 0 meV/f.u., and the distortion amplitudes are obtained by decomposing the distorted structures with respect to $I4/mmm$ and are reported for a 36-atom computational cell.

Irrep	Direction	Space group (N°)	Amplitude (\AA)	Lattice parameters (\AA)			Energy (meV/f.u.)
				a	b	c	
Γ_5^-	$(a, 0)$	$Imm2$ (44)	1.47	5.472	5.472	16.575	154.54
	(a, a)	$Fmm2$ (42)	1.25	5.504	5.461	16.436	133.91
X_2^+	$(a, 0)$	$Bbcm$ (64)	1.31	5.290	5.290	16.646	231.32
	(a, a)	$P4/mbm$ (127)	0.80	5.349	5.349	16.524	310.16
X_3^+	$(a, 0)$	$Bbcm$ (64)	1.48	5.368	5.395	16.663	178.40
	(a, a)	$P4_2/ncm$ (138)	1.51	5.393	5.393	16.576	161.40

TABLE A2. Principal axes of the magnetocrystalline anisotropy energy surfaces for each of the switching steps shown in Figure 5.

Switching figure	Phase	Wyckoff site	Principal axes		
			x	y	z
5(a)	$P2_1ab$	4a	[1.0 -0.2 0.0]	[0.2 0.9 0.3]	[-0.1 -0.3 0.9]
	$Cm2a$	4c	[0.7 -0.7 0.0]	[0.6 0.6 -0.5]	[-0.3 -0.3 -0.9]
	$P2_1ab$	4a	[-0.2 1.0 0.0]	[-0.9 -0.2 -0.3]	[-0.3 -0.1 0.9]
	$Cm2a$	4b	[0.7 -0.7 0.0]	[-0.7 -0.7 -0.3]	[0.2 0.2 -0.9]
	$P2_1ab$	4a	[-1.0 0.2 0.0]	[0.2 0.9 0.3]	[0.1 0.3 -0.9]
5(b)	$P2_1ab$	4a	[1.0 -0.2 0.0]	[0.2 0.9 0.3]	[-0.1 -0.3 0.9]
	$C2$	2b	[0.7 -0.7 0.0]	[-0.7 -0.7 -0.3]	[0.2 0.2 -1.0]
	$P2_1ab$	4a	[-0.2 1.0 0.0]	[-0.9 -0.2 -0.3]	[-0.3 -0.1 0.9]
	Cm	2a	[-0.7 0.7 0.0]	[-0.6 -0.6 -0.4]	[-0.3 -0.3 0.9]
	$P2_1ab$	4a	[-1.0 0.2 0.0]	[0.2 0.9 0.3]	[0.1 0.3 -0.9]

- ⁷ A. K. Boudalis, J. Robert, and P. Turek, *Chem. Eur. J.* **24**, 14896 (2018).
- ⁸ J. Liu, J. Mrozek, W. K. Myers, G. A. Timco, R. E. Winpenny, B. Kintzel, W. Plass, and A. Ardavan, *Phys. Rev. Lett.* **122**, 037202 (2019).
- ⁹ M. Fittipaldi, A. Cini, G. Annino, A. Vindigni, A. Caneschi, and R. Sessoli, *Nat. Mater.* **18**, 329 (2019).
- ¹⁰ J. Liu, V. V. Laguta, K. Inzani, W. Huang, S. Das, R. Chatterjee, E. Sheridan, S. M. Griffin, A. Ardavan, and R. Ramesh, *Sci. Adv.* **7**, eabf8103 (2021).
- ¹¹ A. I. Johnson, F. Islam, C. M. Canali, and M. R. Pederson, *J. Chem. Phys.* **151**, 4 (2019).
- ¹² V. I. Utkin, Y. E. Roginskaya, V. I. Voronkova, V. K. Yanovskii, B. Sh. Galyamov, and Y. N. Venevtsev, *Phys. Stat. Sol. (a)* **59**, 75 (1980).
- ¹³ T. Jardiel, A. C. Caballero, and M. Villegas, *J. Ceram. Soc. Japan* **116**, 511 (2008).
- ¹⁴ M. Campanini, M. Trassin, C. Ederer, R. Erni, and M. D. Rossell, *ACS Appl. Elect. Mater.* **1**, 1019 (2019).
- ¹⁵ C.-P. De Araujo, J. Cuchiaro, L. McMillan, M. Scott, and J. Scott, *Nature* **374**, 627 (1995).
- ¹⁶ X. Mao, W. Wang, X. Chen, and Y. Lu, *Appl. Phys. Lett.* **95**, 1 (2009).
- ¹⁷ L. Keeney, T. Maity, M. Schmidt, A. Amann, N. Deepak, N. Petkov, S. Roy, M. E. Pemble, and R. W. Whatmore, *J. Am. Ceram. Soc.* **96**, 2339 (2013).
- ¹⁸ X. Chen, J. Xiao, Y. Xue, X. Zeng, F. Yang, and P. Su, *Cera. Int.* **40**, 2635 (2014).
- ¹⁹ J. Wang, Z. Fu, R. Peng, M. Liu, S. Sun, H. Huang, L. Li, R. J. Knize, and Y. Lu, *Mater. Horiz.* **2**, 232 (2015).
- ²⁰ Z. Li, J. Ma, Z. Gao, G. Viola, V. Koval, A. Mahajan, X. Li, C. Jia, C. Nan, and H. Yan, *Dalton Trans.* **45**, 14049 (2016).
- ²¹ L. Keeney, S. Kulkarni, N. Deepak, M. Schmidt, N. Petkov, P. F. Zhang, S. Cavill, S. Roy, M. E. Pemble, and R. W. Whatmore, *J. Appl. Phys.* **112**, 0 (2012).
- ²² K. Moore, E. O'Connell, S. M. Griffin, L. Keeney, C. Downing, M. Schmidt, V. Nicolosi, U. Bangert, and M. Conroy, *Research Square* (2021).
- ²³ A. Y. Birenbaum and C. Ederer, *Phys. Rev. B* **90**, 214109 (2014).
- ²⁴ X. Zhai, A. J. Grutter, Y. Yun, Z. Cui, and Y. Lu, *Phys. Rev. Materials* **2**, 044405 (2018).
- ²⁵ A. Faraz, T. Maity, M. Schmidt, N. Deepak, S. Roy, M. E. Pemble, R. W. Whatmore, and L. Keeney, *J. Amer. Ceram. Soc.* **100**, 975 (2017).
- ²⁶ R. Machado, M. G. Stachiotti, R. L. Migoni, and A. Huanosta Tera, *Phys. Rev. B* **70**, 214112 (2004).
- ²⁷ C. E. Mohn and S. Stølen, *Phys. Rev. B* **83**, 014103 (2011).
- ²⁸ H. Djani, E. Bousquet, A. Kellou, and P. Ghosez, *Phys. Rev. B* **86**, 054107 (2012).
- ²⁹ C. Wang, X. Ke, J. J. J. Wang, R. Liang, Z. Luo, Y. Tian, D. Yi, Q. Zhang, J. J. J. Wang, X. F. Han, G. Van Tendeloo, L. Q. Chen, C. W. Nan, R. Ramesh, and J. Zhang, *Nat. Comm.* **7**, 1 (2016).
- ³⁰ H. Okudera, Y. Sakai, K. Yamagata, and H. Takeda, *Acta Crystallogr. Sec. B* **74**, 295 (2018).
- ³¹ N. A. McDowell, K. S. Knight, and P. Lightfoot, *Chem. Eur. J.* **12**, 1493 (2006).

- ³² S. P. Beckman, X. Wang, K. M. Rabe, and D. Vanderbilt, *Phys. Rev. B* **79**, 144124 (2009).
- ³³ J. Heron, J. Bosse, Q. He, Y. Gao, M. Trassin, L. Ye, J. Clarkson, C. Wang, J. Liu, S. Salahuddin, *et al.*, *Nature* **516**, 370 (2014).
- ³⁴ E. A. Nowadnick and C. J. Fennie, *Phys. Rev. B* **94**, 104105 (2016).
- ³⁵ G. Kresse and J. Hafner, *Phys. Rev. B* **47**, 558 (1993).
- ³⁶ G. Kresse and J. Hafner, *Phys. Rev. B* **49**, 14251 (1994).
- ³⁷ G. Kresse and J. Furthmüller, *Comp. Mater. Sci.* **6**, 15 (1996).
- ³⁸ G. Kresse and J. Furthmüller, *Phys. Rev. B* **54**, 11169 (1996).
- ³⁹ P. E. Blöchl, *Phys. Rev. B* **50**, 17953 (1994).
- ⁴⁰ G. Kresse and D. Joubert, *Phys. Rev. B* **59**, 1758 (1999).
- ⁴¹ J. P. Perdew, A. Ruzsinszky, G. I. Csonka, O. A. Vydrov, G. E. Scuseria, L. A. Constantin, X. Zhou, and K. Burke, *Phys. Rev. Lett.* **100**, 136406 (2008).
- ⁴² G. Henkelman, B. P. Uberuaga, and H. Jónsson, *J. Chem. Phys.* **113**, 9901 (2000).
- ⁴³ S. L. Dudarev, G. A. Botton, S. Y. Savrasov, C. J. Humphreys, and A. P. Sutton, *Phys. Rev. B* **57**, 1505 (1998).
- ⁴⁴ H. Stokes, D. Hatch, and B. Campbell. ISOTROPY software suite, <http://stokes.byu.edu/isotropy.html>.
- ⁴⁵ K. Momma and F. Izumi, *J. Appl. Crystallogr.* **41**, 653 (2008).
- ⁴⁶ A. Glazer, *Acta Crystallogr. Sec. B* **28**, 3384 (1972).
- ⁴⁷ A. D. Rae, J. G. Thompson, and R. L. Withers, *Acta Crystallogr. Sec. B* **47**, 870 (1991).
- ⁴⁸ A. Schrön, C. Rödl, and F. Bechstedt, *Phys. Rev. B* **86**, 115134 (2012).
- ⁴⁹ I. G. Rau, S. Baumann, S. Rusponi, F. Donati, S. Stepanow, L. Gragnaniello, J. Dreiser, C. Piamonteze, F. Nolting, S. Gangopadhyay, *et al.*, *Science* **344**, 988 (2014).
- ⁵⁰ J.-X. Yu and J. Zang, *Sci. Adv.* **4**, eaar7814 (2018).
- ⁵¹ M. Ležaić and N. A. Spaldin, *Phys. Rev. B* **83**, 024410 (2011).
- ⁵² P. C. Rout and U. Schwingenschlögl, *Nano Lett.* **21**, 6807 (2021).
- ⁵³ J. Zhou, Q. Wang, Q. Sun, Y. Kawazoe, and P. Jena, *Physical Chemistry Chemical Physics* **17**, 17182 (2015).
- ⁵⁴ M. Ye and D. Vanderbilt, *Phys. Rev. B* **93**, 134303 (2016).
- ⁵⁵ Z. Liao, M. Huijben, Z. Zhong, N. Gauquelin, S. Macke, R. Green, S. Van Aert, J. Verbeeck, G. Van Tendeloo, K. Held, *et al.*, *Nat. Mater.* **15**, 425 (2016).
- ⁵⁶ D. Yi, C. L. Flint, P. P. Balakrishnan, K. Mahalingam, B. Urwin, A. Vailionis, P. Shafer, E. Arenholz, Y. Choi, K. H. Stone, *et al.*, *Phys. Rev. Lett.* **119**, 077201 (2017).
- ⁵⁷ J. Perez-Mato, M. Aroyo, A. García, P. Blaha, K. Schwarz, J. Schweifer, and K. Parlinski, *Phys. Rev. B* **70**, 214111 (2004).
- ⁵⁸ N. A. Benedek and C. J. Fennie, *Phys. Rev. Lett.* **106**, 107204 (2011).